Application of the Bilateral Filter for the Reconstruction of Spiral Bevel Gear Tooth Surfaces From Point Clouds

Ignacio Gonzalez-Perez[1]
Department of Mechanical Engineering,
Materials and Manufacturing,
Universidad Politécnica de Cartagena,
Cartagena 30202, Spain
e-mail: ignacio.gonzalez@upct.es

Pedro L. Guirao-Saura
Department of Mechanical Engineering,
Materials and Manufacturing,
Universidad Politécnica de Cartagena,
Cartagena 30202, Spain
e-mail: pedro.guirao@upct.es

Alfonso Fuentes-Aznar
Department of Mechanical Engineering,
Rochester Institute of Technology,
Rochester, NY 14623
e-mail: afeme@rit.edu

Reconstruction of gear tooth surfaces from point clouds obtained by noncontact metrology machines constitutes a promising step forward not only for a fast gear inspection but also for reverse engineering and virtual testing and analysis of gear drives. In this article, a new methodology to reconstruct spiral bevel gear tooth surfaces from point clouds obtained by noncontact metrology machines is proposed. The need of application of a filtering process to the point clouds before the process of reconstruction of the gear tooth surfaces has been revealed. Hence, the bilateral filter commonly used for 3D object recognition has been applied and integrated in the proposed methodology. The shape of the contact patterns and the level of the unloaded functions of transmission errors are considered as the criteria to select the appropriate settings of the bilateral filter. The results of the tooth contact analysis of the reconstructed gear tooth surfaces show a good agreement with the design ones. However, stress analyses performed with reconstructed gear tooth surfaces reveal that the maximum level of contact pressures is overestimated. A numerical example based on a spiral bevel gear drive is presented. [DOI: 10.1115/1.4048219]

Keyword: gear geometry

1 Introduction

Reconstruction of gear tooth surfaces from coordinate measurement through a contact metrology was presented in Ref. [1] for gear inspection and computerized simulation of meshing. A noncontact methodology for gear inspection was proposed in Ref. [2] through a laser holographic measurement. Nowadays, reconstruction of gear tooth surfaces from point clouds obtained throughout the use of noncontact metrology machines constitutes a promising step forward not only to perform the traditional gear inspection process but also to apply virtual testing and simulation of the to-be inspected gears by means of the tooth contact analysis (TCA) and the stress analysis. Noncontact metrology machines allow a fast measurement of a whole gear in few minutes. However, one of the main drawbacks of laser noncontact metrology machines at this moment is the precision and dispersion of the measured points that form the point cloud of the gear tooth surfaces. Such a dispersion is a general behavior in 3D scanners as it is revealed in Ref. [3].

Some previous publications consider the raw data provided by noncontact metrology machines [4–6], mainly point clouds for gear inspection, tooth contact analysis, and stress analysis of the reconstructed gear drives. However, the deficiency in the results obtained from tooth contact and stress analysis is revealed in Refs. [5,6], demanding the application of filters to the point cloud.

Filtering of point clouds is an usual technique that is being applied in 3D object recognition to reduce the noise and preserve the shape of a being-inspected object. First applications of surface reconstruction from unorganized points can be found in Ref. [7] where the underlying theory to get the tangent plane at a given point of the sough-for surface was introduced. Such a plane constitutes the regression plane of the neighboring points to the given point of the point cloud. In Ref. [8], the bilateral filter proposed in Ref. [9] for image processing is adapted for mesh reconstruction, although the normal to the tangent plane is not obtained as it is proposed in Ref. [7], but from triangulation between points of the first ring in the neighborhood. Here, in Ref. [8], the Euclidean distance of the neighboring points to the given point and the normal distance to the tangent plane are considered in the equation to denoise each given point, considering Gaussian functions to weigh the contribution of such distances. Later, in Ref. [10], the bilateral filter is adapted considering the determination of the normal to the tangent plane as it was presented in Ref. [7], proposing the use of a function of the sphere radius, which determines the size of the neighborhood, for the variances in the Gaussian functions.

This article establishes a methodology to reconstruct spiral bevel gear tooth surfaces from filtered point clouds by using the bilateral filter. The active tooth surfaces are successfully reconstructed from the obtained point clouds after the application of the proposed methodology. However, due to the poor quality of the point cloud in the fillet areas, these areas are reconstructed throughout the application of Hermite curves that approach these curves to the available cloud points in such areas. This does not diminish the proposed methodology of reconstruction that can be easily extended to the fillet areas as soon as the point data would be available. Conversely, the aim of this article is to prove the effectiveness of the bilateral filter to reconstruct gear tooth surfaces and to perform tooth contact and stress analysis of gear drives with the reconstructed gear tooth surfaces. Furthermore, some criteria are established for the application of the bilateral filter based on the results of the tooth contact analysis. Basically, the shape of the contact pattern, the unloaded function of transmission errors, and the level of the unloaded transmission errors are taken into account to judge whether the parameters of the bilateral filter are appropriate for the reconstructed gear. However, stress analysis by application of the finite element models shows that the technology of noncontact metrology machines require improvements to approach contact stresses in

[1]Corresponding author.

Contributed by the Power Transmission and Gearing Committee of ASME for publication in the Journal of Mechanical Design. Manuscript received March 12, 2020; final manuscript received July 27, 2020; published online xx xx, xxxx. Assoc. Editor: Mohsen Kolivand.

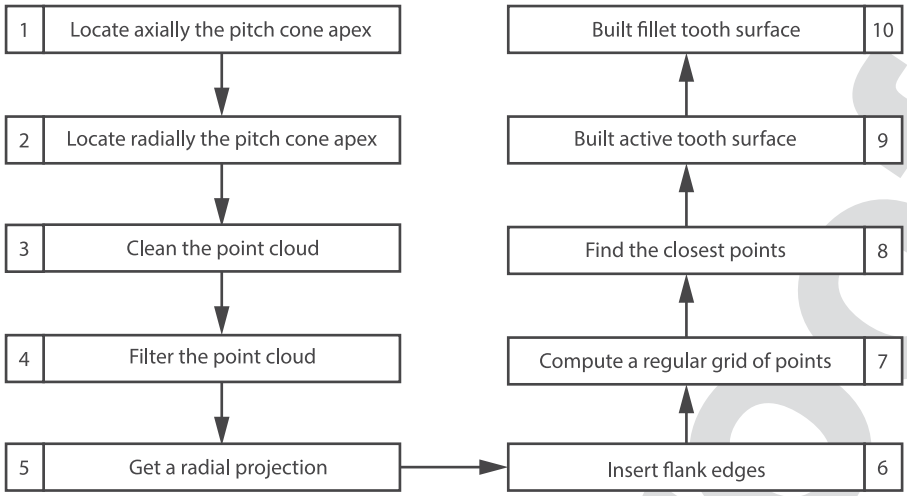

Fig. 1 Summary diagram of the proposed methodology to reconstruct spiral bevel gear tooth surfaces

reconstructed geometries to those obtained from computational gear generation of the design gears.

A numerical example of a spiral bevel gear drive is considered later in this study. The design and manufacturing data of the spiral bevel gears are known. A spiral bevel pinion, once it has been manufactured and inspected, is reconstructed following the procedure described in this article. Then, it will be considered in virtual meshing with a *master* spiral bevel gear. The results prove the effectiveness of the bilateral filter to reproduce, with the reconstructed pinion tooth surfaces, similar contact patterns, and unloaded transmission errors to those obtained with computationally generated gear tooth surfaces. The reconstruction is performed with the point clouds for both tooth sides of just a tooth, leaving the reconstruction of all the gear teeth for future research.

2 Reconstruction of Gear Tooth Surfaces

Reconstruction of a gear tooth from point clouds obtained by a noncontact metrology machine requires the application of the process described later. A summary diagram is visualized in Fig. 1.

Step 1: The axial location of the pitch cone apex Q of the to-be reconstructed gear is determined. Figure 2 shows the to-be inspected gear, the point clouds corresponding to each tooth side, and the point cloud corresponding to the back side of the gear that need to be inspected. These points on the back side of the gear approach a plane that can be designated here as *back plane*. Figure 2 shows a well coordinate system S_m where point coordinates of all the point clouds are obtained. Point O_m represents the origin for the measurements of the noncontact metrology machine. Location of the pitch cone apex in the axial direction means to determine the coordinate $z_m^{(Q)}$ in system S_m. Such a coordinate can be obtained as follows:

$$z_m^{(Q)} = z_{plane} + m_d \tag{1}$$

where z_{plane} is the mean value of coordinates z of the point cloud that approaches the *back plane* and m_d is the so-called mounting distance. The value of the mounting distance is required in this procedure. Otherwise, the location of the gear in its virtual assembly with a master gear would require a trial and error process since the origin O_m do not have to coincide with the pitch cone apex.

Figure 2 also shows the coordinate system S_g where the to-be reconstructed gear will be defined. The origin of system S_g is located at the pitch cone apex Q. A coordinate transformation from system S_m to system S_g is required. It is suggested to perform that at step 10 once the reconstructed gear tooth surfaces have been obtained.

Step 2: The radial location of the pitch cone apex Q of the to-be reconstructed gear is determined. Figure 3 shows the point clouds corresponding to each tooth side and the point cloud corresponding to an internal cylinder of the gear to be inspected. The axis of such a cylinder is the axis where point Q is located. Such an axis may not pass through the origin of the coordinate system S_m since some position error Δr_m may exist. To determine it, a least-square minimization problem is established following the Levenberg–Marquardt algorithm [11,12] where the objective function

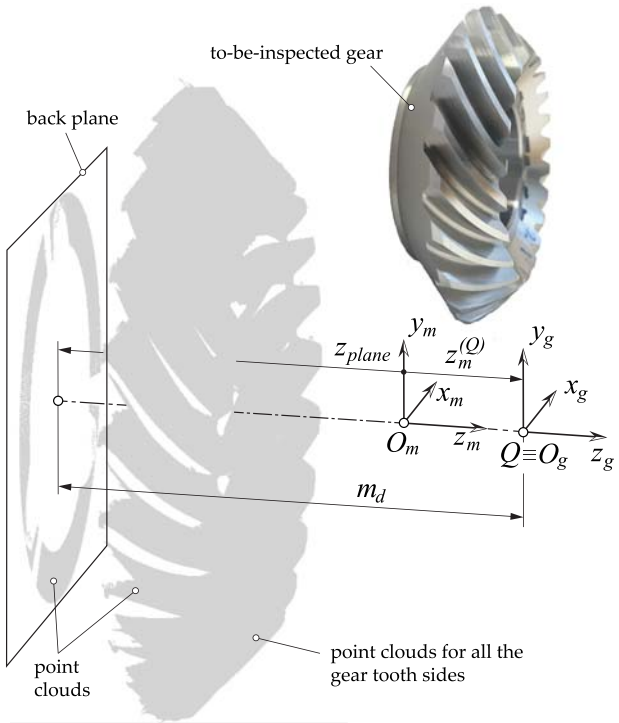

Fig. 2 Illustration of coordinate systems S_m where point clouds are obtained and S_g where the to-be reconstructed gear is defined

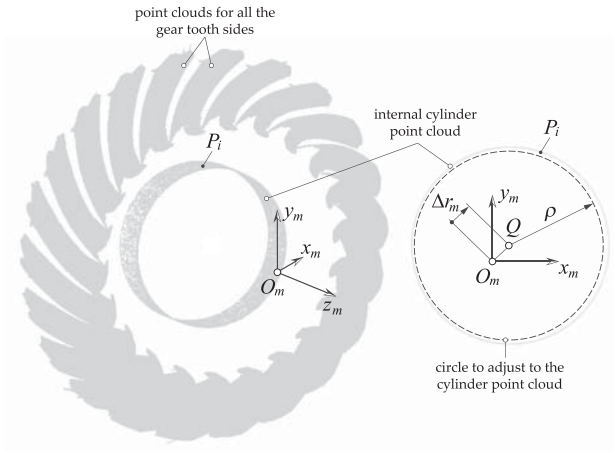

Fig. 3 For determination of a circle that adjusts to the internal cylinder point cloud in the plane (x_m, y_m) and position error Δr_m for the location of pitch cone apex Q

is defined as follows:

$$f(\mathbf{x}) = \sum_{i=1}^{m} [(x_m^{(P_i)} - \Delta r_{m,x})^2 + (y_m^{(P_i)} - \Delta r_{m,y})^2 - \rho^2] \quad (2)$$

where $\mathbf{x} = [\Delta r_{m,x}, \Delta r_{m,y}, \rho]$ is the vector of optimization variables, where $\Delta r_{m,x}$ and $\Delta r_{m,y}$ allow the determination of the radial location of point Q and ρ is the radius of a circle that adjusts to the cylinder point cloud in the plane (x_m, y_m). Conversely, $(x_m^{(P_i)}, y_m^{(P_i)})$ represent the coordinates of any point P_i of the cylinder point cloud in the coordinate system S_m. The objective function is constructed on the m points of the cylinder point cloud. Just one of the variables is restricted to be positive

$$0 \leq \rho \quad (3)$$

An additional coordinate transformation may be required from system S_m to system S_g in case $\Delta r_{m,x} \neq 0$ or $\Delta r_{m,y} \neq 0$. It is suggested to perform that at step 10 once the reconstructed gear tooth surfaces have been obtained.

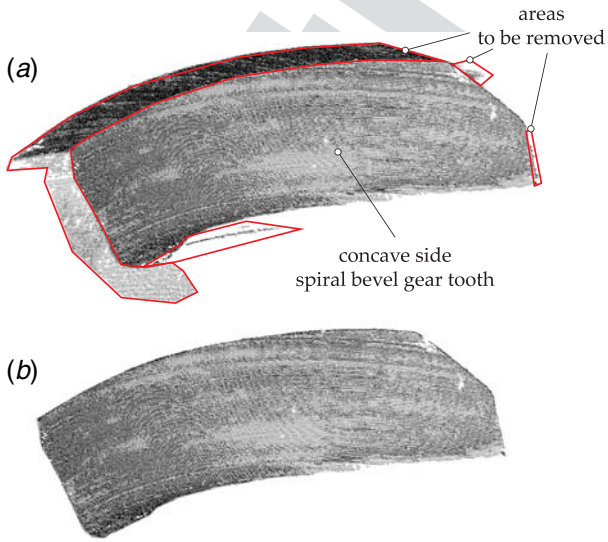

Fig. 4 Cleaning the point clouds: (*a*) point cloud before cleaning and (*b*) point clouds after cleaning

Step 3: Cleaning the point clouds corresponding to both tooth sides of a given tooth. The point clouds obtained by noncontact metrology machines contain large amounts of points related to different parts of the gear tooth (top land, front and back surfaces of the tooth, and root land) that are not of interest for the reconstruction of the active gear tooth surfaces. Figure 4(*a*) shows the raw point cloud corresponding to the concave side of a spiral bevel gear tooth. Figure 4(*b*) shows such point cloud after removing those points at the mentioned areas of not interest. This task saves time for the next step. The same procedure has to be repeated with the point cloud for the convex tooth side.

Step 4: Filtering of the point clouds is done. The bilateral filter approach is applied by using the following algorithm (see Ref. [10] for more details):

(a) A spatial radius r, a normal offset r_n, and a number of iterations n_{iter} are chosen as input data for the algorithm. Variable r represents the radius of a sphere to obtain the neighbors for each given point $\mathbf{p}$ of the point cloud. Variable r_n represents an offset value in both directions of a to-be calculated normal $\mathbf{n}_p$ at the point $\mathbf{p}$. Variable n_{iter} represents the number of iterations the algorithm is applied. At the end of each iteration, the points of the point cloud are located in new positions.

(b) Neighbors $\mathbf{p}_i$ of point $\mathbf{p}$ are determined using a kd-structure of the points [13] to find those points, where $\| \mathbf{p}_i - \mathbf{p} \| < r$. Then, the unit normal $\mathbf{n}_p$ is calculated from the locations of the neighbors as follows:

(i) A mean value of the neighbors or centroid $\mathbf{c}_p$ is determined as follows:

$$\mathbf{c}_p = \frac{1}{N_p} \sum_{i=1,N_p} \mathbf{p}_i \quad (4)$$

where N_p is the number of neighbors of point $\mathbf{p}$ inside the sphere of radius r.

(ii) A matrix $\mathbf{A}$ is determined for each point $\mathbf{p}$ considering the locations of the neighbors $\mathbf{p}_i$

$$\mathbf{A} = \frac{1}{N_p} \sum_{i=1,N_p} (\mathbf{p}_i - \mathbf{c}_p) \cdot (\mathbf{p}_i - \mathbf{c}_p)^T \quad (5)$$

(iii) The normal $\mathbf{n}_p$ is obtained as the eigenvector corresponding to the minimum eigenvalue λ_{min} of such a matrix $\mathbf{A}$ since

$$(\mathbf{x} - \mathbf{c}_p) \cdot \mathbf{n}_p = 0 \quad (6)$$

represents a plane that minimize the sum of squared distances between the plane and the neighbors $\mathbf{p}_i$.

(c) Each point $\mathbf{p}$ is filtered using the following equation:

$$\mathbf{p}' = \mathbf{p} + \delta p \cdot \mathbf{n}_p \quad (7)$$

where

$$\delta p = \frac{\sum_{i=1,N_p} w_d(\| \mathbf{p}_i - \mathbf{p} \|) w_n((\mathbf{p}_i - \mathbf{p}) \cdot \mathbf{n}_p)(\mathbf{p}_i - \mathbf{p}) \cdot \mathbf{n}_p}{\sum_{i=1,N_p} w_d(\| \mathbf{p}_i - \mathbf{p} \|) w_n((\mathbf{p}_i - \mathbf{p}) \cdot \mathbf{n}_p)} \quad (8)$$

Here, w_d and w_n are decreasing Gaussian functions, which are defined as follows:

$$w_d(x) = e^{-x^2/2\sigma_d^2} \quad (9)$$

$$w_n(x) = e^{-x^2/2\sigma_n^2} \quad (10)$$

Here, σ_d^2 is the Gaussian variance for the distance from the neighbor $\mathbf{p}_i$ to point $\mathbf{p}$, whereas σ_n^2 is the Gaussian variance for the distance from the neighbor $\mathbf{p}_i$ to the tangent plane defined by normal $\mathbf{n}_p$. The Gaussian variances σ_d^2 and σ_n^2

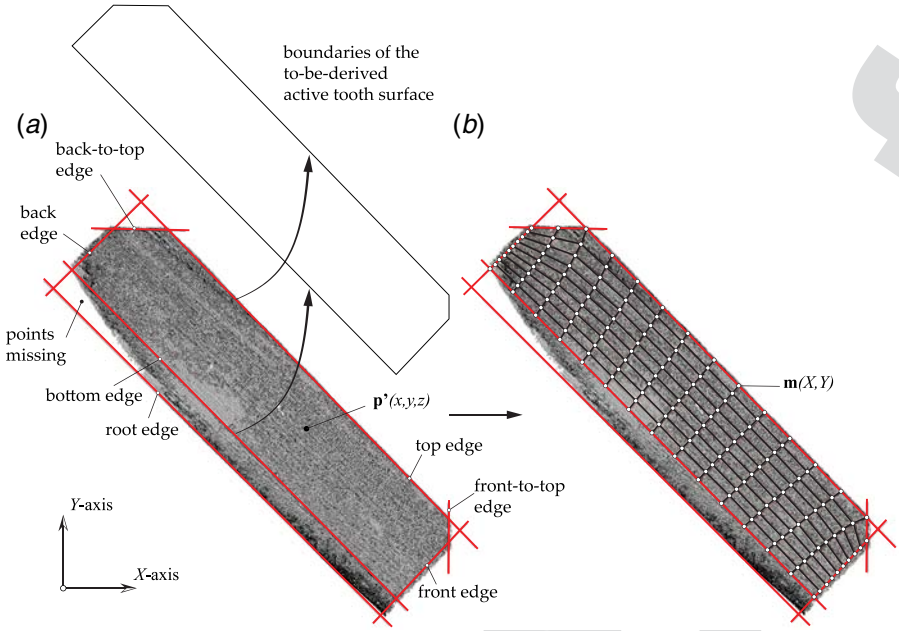

Fig. 5 Radial projection of the filtered point cloud with illustration of (*a*) flank edges and (*b*) computed grid for a spiral bevel gear tooth

are fixed considering $\sigma_d = r/3$ and $\sigma_n = r_n/3$ since for those neighbors $\mathbf{p}_i$ whose distance is beyond $3\sigma_d$ and normal distance is beyond $3\sigma_n$, the weights w_d and w_n are negligible (see Ref. [10]).

(d) Steps b and c are repeated several times depending on the chosen value of number of iterations, n_{iter}.

Step 5: This is the representation of the *radial* projection of the point cloud considering a plane formed by an axis X directed along the gear axis and an axis Y that represents the radial distance of each point of the point cloud. Figure 5(*a*) shows a radial projection of the filtered point cloud where points $\mathbf{p}'(x, y, z)$ are represented through the following relations:

$$X(\mathbf{p}') = z \tag{11}$$

$$Y(\mathbf{p}') = \sqrt{x^2 + y^2} \tag{12}$$

Step 6: Definition of the flank edges on the radial projection of the point cloud is presented. These flank edges are based on a top edge, a bottom edge, a root edge, a front edge, and a back edge. In addition, a back-to-top edge and a front-to-top edge can be considered as being illustrated in Fig. 5(*a*) for the case of a spiral bevel gear tooth surfaces in which the back-top and front-top corners have been cut off. The flank edges can be defined considering that the to-be derived active tooth surface has to be delimited by all these edges with the exception of the root edge. Figure 5(*a*) also shows that some points are missing in the point cloud, which may force the location of the bottom edge for the to-be derived active tooth surface to have points where a radial grid can be created.

Step 7: Creation of a grid of $m \times n$ points on the radial projection is carried out as shown in Fig. 5(*b*). Points $\mathbf{m}(X, Y)$ are obtained from a regular grid defined by the aforementioned edges delimiting the to-be derived active tooth surface.

Step 8: The closest point of the point cloud for each point $\mathbf{m}(X, Y)$ of the radial grid is found. This closest point of the point

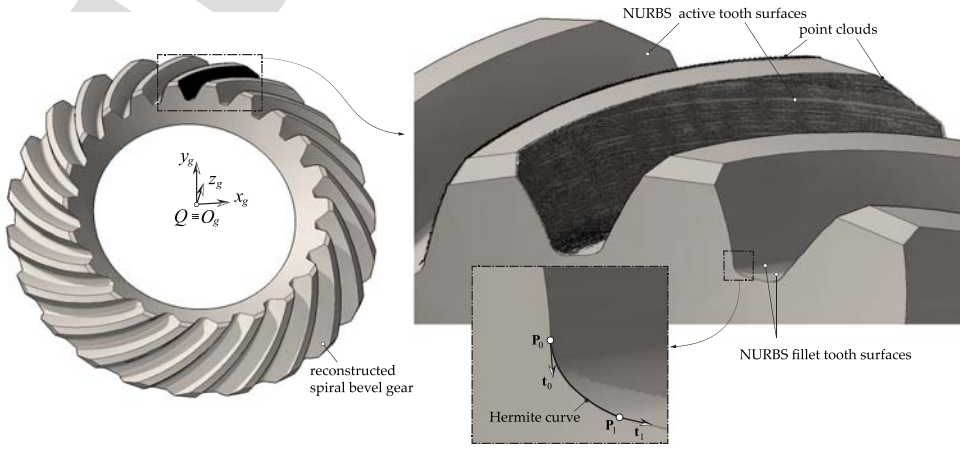

Fig. 6 Reconstructed spiral bevel gear from filtered point clouds

cloud can be found using a kd-tree structure of the points [13].

Step 9: A NURBS (nonuniform rational B-splines) surface [14] is built considering the obtained points in the previous step as control points. Most of the graphic libraries include this feature to interpolate a regular grid of points through a second-order derivative surface. This surface constitutes the active tooth surface of the gear tooth.

Step 10: The fillet surface is built to entrench the bottom edge of the active tooth surface with the root edge. Hermite curves are applied here for the determination of the control points that will allow to build a NURBS surface for the fillet area. Hermite curves require basically the initial and final point positions, the initial and final unit tangents, and the weights (or modules) of such tangent vectors (see Ref. [15] for a complete review of application of Hermite curves in fillet construction). The initial point and initial unit tangent can be derived from the active tooth surface. The final point and final unit tangent can be derived from the location of the root edge on the radial projection and the angular pitch $2\pi/N_g$ of the gear. Here, N_g is the tooth number of the to-be inspected gear that is considered as known. The weights are derived through an optimization process that follows the Levenberg–Marquardt algorithm [11,12] and minimizes the sum of distances of a sample of cloud points in the fillet area to the to-be computed NURBS surface.

Figure 6 shows a reconstructed spiral bevel gear with the illustration of the NURBS surfaces for the concave and convex tooth sides and the NURBS surfaces of the fillet areas. Here, a detail view of an Hermite curve is illustrated as well on the front section, where P_0 is the initial point, $\mathbf{t}_0$ is the unit initial tangent, P_1 is the final point, and $\mathbf{t}_1$ is the unit final tangent.

3 Tooth Contact and Stress Analysis

In this work, TCA is applied for a reconstructed spiral bevel pinion in mesh with a master spiral bevel gear. The TCA algorithm is based on the work [16] and has been applied later in Refs. [17,18]. It is based on the minimization of the distance between the master gear driven tooth surface and the reconstructed pinion driving tooth surface. It considers the surfaces as rigid, so that it is necessary to set a value for the so-called *virtual marking compound thickness* t_v, which is usually fixed to 0.0065 mm, to obtain the contact pattern and the unloaded function of transmission errors. Figure 7 shows

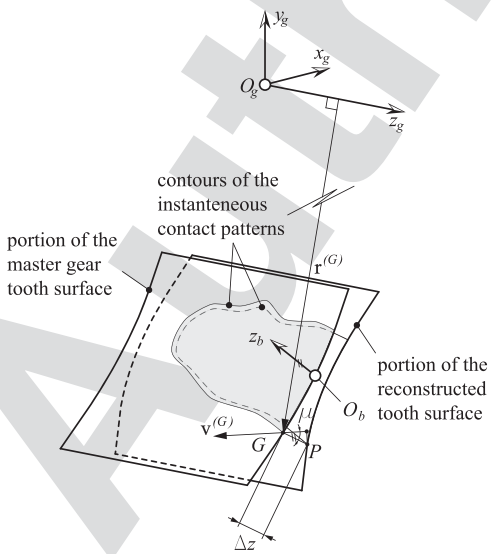

Fig. 7 Schematic view for the explanation of the minimization of distances between the master gear tooth surface and the reconstructed pinion tooth surface

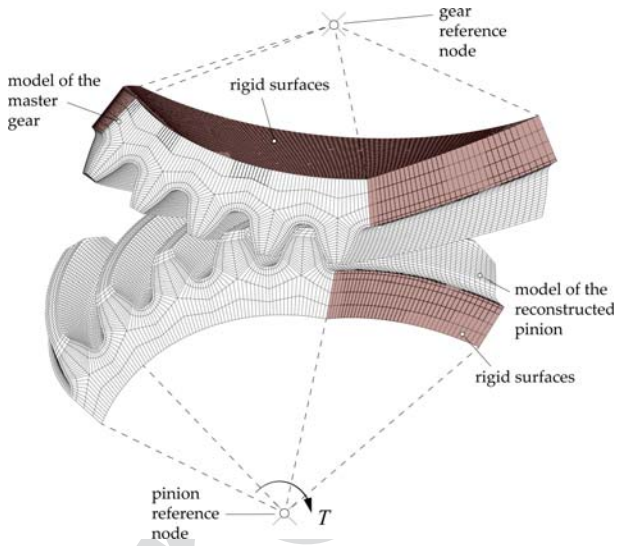

Fig. 8 Finite element model

both surfaces at a given step of the algorithm. A coordinate system S_b is predefined in the master gear tooth surface with its axis z_b directed along the normal at a given point O_b on the middle of the surface. For each given position of the reconstructed tooth surface, distance $\Delta z\cos\mu$ is minimized by approaching the master gear tooth surface toward the reconstructed tooth surface. Such a distance is obtained following a kinematic procedure, as it is explained in Ref. [16], using the direction of velocity vector $\mathbf{v}^{(G)}$ at point G. Point G is obtained from the projection of point P of the reconstructed tooth surface on the master tooth surface. A set of points like P are taken from a grid of points for the application of the algorithm. Angle μ is formed by the directions of vector $-\mathbf{v}^{(G)}$ and GP. Once the contact is established, those points like P and G whose distance Δz is equal to the given value t_v form the contours of the instantaneous contact patterns.

In previous works where TCA was applied in reconstructed gear tooth surfaces (see Refs. [5,6]), the value of t_v had to be increased to be able to obtain acceptable contact patterns. An *acceptable* contact pattern means that the contact pattern present a regular shape with no holes or isolated areas. The need to increase t_v was due to the irregularities of the NURBS surfaces since filtering approaches were not applied. In this study, the magnitude of t_v will be fixed to 0.0065 mm, as it has been set in the previous study (see Ref. [19]), where TCA was applied with theoretically generated gear tooth surfaces, and the results of the filtering approaches will be judged in terms of the shape of the contact pattern and the level of the function of transmission errors.

Conversely, the stress analysis is based on the application of the finite element method and constitutes another tool to judge the goodness of the filtering approach. A finite element model is illustrated in Fig. 8, which is built with elements C3D8I (see Ref. [20]). The foundation for the construction of the finite element model is found in Ref. [19]. The nodes on the bottom part and both sides of the rim of each gear constitute rigid surfaces that are rigidly connected to the respective reference nodes. Here, at the reference nodes, the degrees-of-freedom are established. Although the gear is held at rest at each given contact position, a torque T is applied to the pinion reference node. It is observed that the model of the reconstructed pinion is provided with additional flank edges on the toe and the heel top corners. To evaluate the quality of the reconstructed gear tooth surfaces for the stress analysis, the maximum contact pressure at the middle tooth of the reconstructed pinion will be obtained along two cycles of meshing and compared with the maximum contact pressures obtained with the designed and manufactured pinion, all in mesh with the same master spiral bevel gear.

4 Numerical Example

A numerical example is being considered based on a known design of a spiral bevel pinion and gear, both manufactured in a Phoenix II 275G machine. Furthermore, the manufactured pinion, for which the machine tool settings are known, has been inspected in a HNC3030 noncontact metrology machine whose precision is ±5 μm. The to-be inspected pinion will be in virtual mesh, after reconstruction, with a *master* gear. Here, the term *master* refers to a gear that has been computationally generated based on its known design.

Once the to-be inspected pinion has been scanned, the reconstruction of the pinion will be performed following the ideas presented in Sec. 2. The proposed approach shown in Sec. 2 will be judged in terms of the shape of the contact pattern, the level of unloaded transmission errors, and the level of contact stresses obtained from the analysis of the reconstructed pinion in mesh with the master gear. Additional information of micro-geometry deviations after manufacturing of the pinion has been obtained by using a coordinate measurement machine GMS350 whose precision is ±1 μm. These micro-deviations can be added to the computationally generated geometry corresponding to the known design of the spiral bevel pinion, obtaining the *virtual manufactured* geometry of the pinion. The results of TCA and stress analysis of the reconstructed spiral bevel pinion in mesh with the master gear can be compared with those obtained from the tooth contact and stress analysis of the *virtual manufactured* geometry of the pinion in mesh with the same master gear.

4.1 Design Data. The design of a spiral bevel gear drive is presented. The basic transmission and blank data are summarized in Table 1. The cutter data and basic machine tool settings are presented in Table 2. A detailed description of the basic machine tool settings is available in Ref. [19].

4.2 Manufactured Data. The averaged micro-geometry deviations for the pinion concave tooth side are given in Table 3 for a grid of 5 × 9 points. Such a grid covers 80% of the tooth surface. Once those micro-deviations are incorporated into the virtual computationally generated pinion, the tooth contact and stress analysis results obtained considering such a pinion in mesh with the master gear will establish the reference baseline results for comparison with those obtained with the reconstructed pinion in mesh with the same master gear.

4.3 Preliminary Tooth Contact Analysis Results. The results of the TCA between the *designed* concave tooth side of the pinion in mesh and the convex tooth side of the master spiral bevel gear is shown in Fig. 9. The results of TCA between the *manufactured* concave tooth side of the pinion in mesh with the same mater gear convex tooth surface is also illustrated in Fig. 9. The level of unloaded transmission errors is about 9 arc-seconds for the designed gear tooth surfaces, whereas it is about 26 arc-seconds when the manufactured pinion tooth surface is used instead of the designed one.

4.4 Tooth Contact Analysis With Reconstructed Gears. The manufactured pinion has been reconstructed considering the procedure described in Sec. 2. At step 1, a mounting distance $m_d = 58.1$ mm and a $z_{plane} = -56.4$ mm provide the value $z_m^{(Q)} = 1.7$ mm to locate the pitch cone apex and the origin of system S_g, where the to-be reconstructed pinion is defined (see Fig. 2). At step 2, the Levenberg–Marquardt algorithm is applied upon $m = 243{,}062$ points of the internal cylinder point cloud to obtain $\Delta r_{m,x} = -1.8182 \times 10^{-5}$ mm, $\Delta r_{m,y} = -4.1794 \times 10^{-6}$ mm and $\rho = 17.175$ mm, which reflects negligible errors in the radial location of the pitch cone apex. A grid of 10 × 15 points has been considered in the radial projection in step 6 for all the cases considered here. The previous study (see Ref. [5]) has shown that a larger amount of grid points may lead to obtain reconstructed surfaces with more irregularities. Figure 6 shows an example of a reconstructed pinion.

Figure 10 represents a comparison of the unloaded functions of transmission errors for the manufactured pinion and a reconstructed pinion without using any filter. The contact patterns are also represented in Fig. 10 as a set of instantaneous contact areas obtained from the procedure exposed in Sec. 3. When no filter is applied,

Table 1 Basic transmission and blank data of the spiral bevel gear drive

Data	Pinion	Gear
Shaft angle (deg)	90.0	
Tooth number	22	23
Pitch angle (deg)	43.727	46.273
Spiral angle (deg)	45.0	
Hand of spiral	Right hand	Left hand
Outer transverse module (mm)	3.7398	
Face width (mm)	18.0	
Tooth taper	Duplex	
Outer addendum (mm)	2.823	2.344
Outer dedendum (mm)	2.906	3.384
Face cone angle (deg)	46.084	48.233
Root cone angle (deg)	41.767	43.916

Table 2 Cutter data and basic machine tool settings of the spiral bevel gear drive

Data	Pinion (concave tooth side)	Gear (convex tooth side)
Cutting method	Face milling	
Cutter type	Fixed setting	Spread blade
Point radius (mm)	46.672	43.701
Blade angle (deg)	17.760	22.0
Blade profile	Circular	Straight
Blade profile radius (mm)	762.0	Not applicable
Bottom relief height (mm)	1.5	1.5
Bottom relief parabola coefficient (mm^{-1})	0.015	0.010
Machine center to back (mm)	−0.493	0.0
Sliding base (mm)	−0.540	−0.934
Blank offset (mm)	0.0100	0.0
Radial distance (mm)	36.220	36.771
Cradle angle (deg)	60.403	58.735
Machine root angle (deg)	41.767	43.916
Velocity ratio	1.4526	1.3826
Modified roll coefficient C	0.006269	Not applicable
Modified roll coefficient D	−0.01633	Not applicable

Table 3 Deviations in μm on the concave tooth side of the manufactured spiral bevel pinion along 5 × 9 grid points

Points along face width/profile	1 (near top edge)	2	3	4	5 (near bottom edge)
1 (near toe)	−2.1	−1.9	0.3	0.2	−1.7
2	−2.0	0.3	0.5	1.1	−1.2
3	−2.1	0.8	0.0	1.5	−1.3
4	0.5	−0.3	0.6	1.2	−2.3
5	−0.6	0.1	0.0	0.0	−3.3
6	−1.2	0.4	0.0	−1.3	−4.3
7	−3.5	−0.6	−1.3	−2.7	−5.7
8	−4.1	−3.6	−3.1	−3.9	−7.3
9 (near heel)	−2.7	−3.9	−3.4	−5.1	−8.3

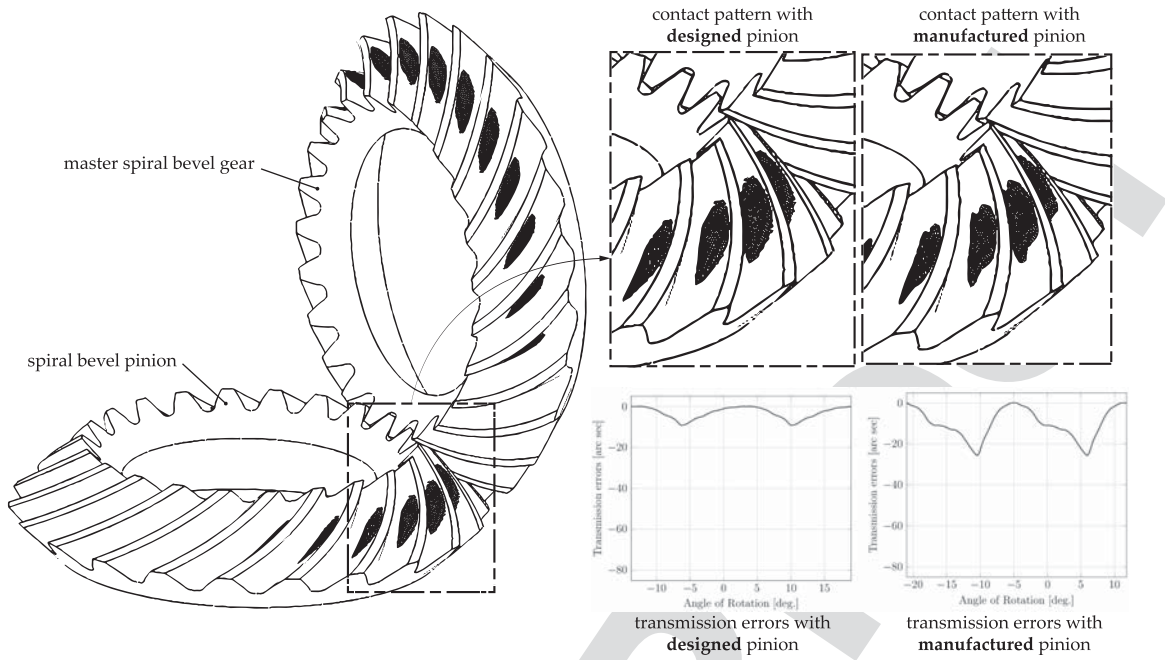

Fig. 9 Contact patterns and unloaded functions of transmission errors for the *designed* and the *virtual manufactured* spiral bevel pinion in mesh with the master spiral bevel gear

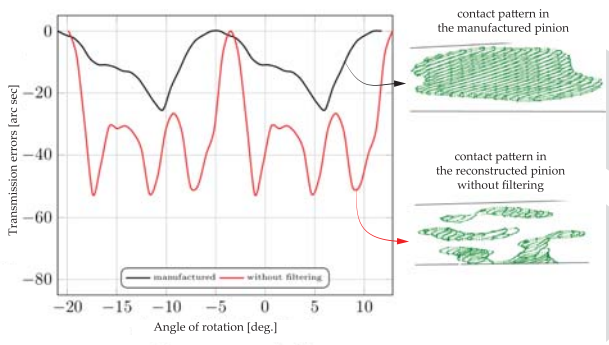

Fig. 10 Contact patterns and unloaded transmission errors for the manufactured pinion and the reconstructed pinion without filtering in mesh with the master gear

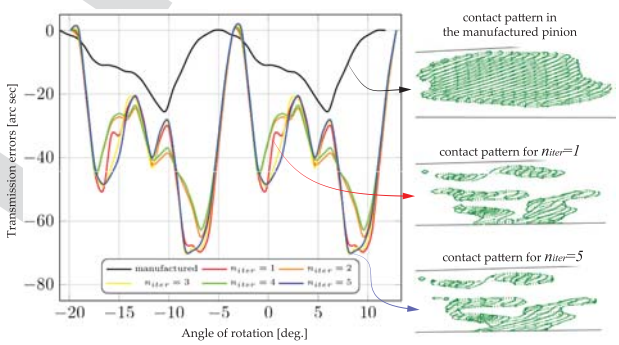

Fig. 11 Contact patterns and unloaded transmission errors for the manufactured pinion and the reconstructed pinions using the bilateral filter with $r = r_n = 25\ \mu$m in mesh with the master gear

the contact pattern of the reconstructed pinion shows isolated areas. Also, the shape of the function of transmission errors and the level of transmission errors are far from the function of transmission errors and the level of transmission errors of the manufactured pinion. These results (Fig. 10) show the need to apply a filter to the point clouds before the reconstruction of the gear tooth surfaces.

The bilateral filter is applied to the point clouds of the manufactured spiral bevel pinion providing different reconstructed pinions for different values of the filter parameters. The first question that arises here is how large the sphere radius r and the offset value r_n should be chosen for a given point cloud. This depends on how the points are distributed all over the point cloud. If the radius is too small, the fitting regression plane could not be enough accurate. A set of values $r = r_n = \{25, 50, 75, 100\}\ \mu$m combined with $n_{iter} = \{1, 2, 3, 4, 5\}$ has been tested to reconstruct 20 spiral bevel pinions. For each reconstructed pinion in mesh with the master gear, TCA is applied.

Figure 11 shows the unloaded functions of transmission errors when the bilateral filter with $r = r_n = 25\ \mu$m is applied. The level of transmission errors for any number of iterations from 1 to 5 is far from the level of transmission errors of the manufactured

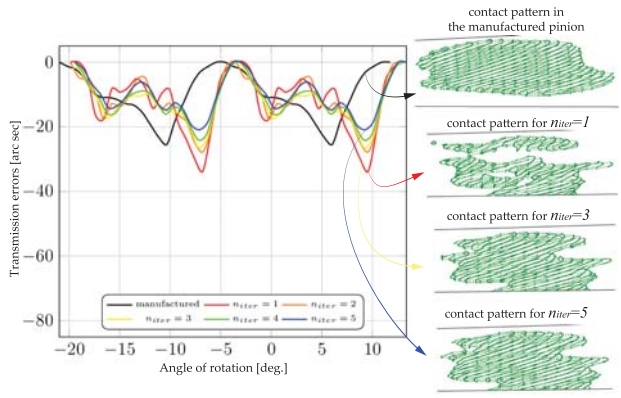

Fig. 12 Contact patterns and unloaded transmission errors for the manufactured pinion and the reconstructed pinions using the bilateral filter with $r = r_n = 100\ \mu$m in mesh with the master gear

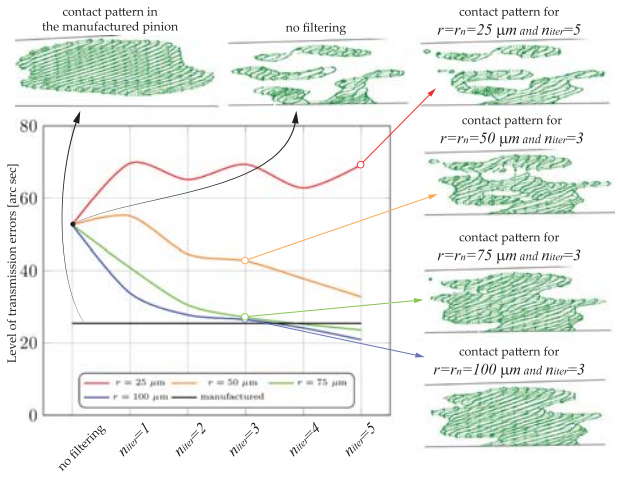

Fig. 13 Contact patterns and level of unloaded transmission errors for the manufactured pinion and the reconstructed pinions using no filter and using the bilateral filter

pinion in mesh with the master gear. The shapes of the contact patterns are also illustrated for $n_{iter}=1$ and $n_{iter}=5$ in Fig. 11. It can be observed that the shape of the contact patterns is also far from the reference shape of the contact pattern corresponding to the manufactured pinion.

Figure 12 shows the unloaded functions of transmission errors when the bilateral filter with $r=r_n=100\,\mu$m is applied. The shapes of the contact patterns are also illustrated for $n_{iter}=1$, $n_{iter}=3$, and $n_{iter}=5$ in Fig. 12. It is observed that the contact pattern with $n_{iter}=1$ presents holes and isolated areas in the formation of the bearing contact. Such features start to disappear from $n_{iter}=3$ on. The minimum number of iterations from which the contact pattern does not present holes or isolated areas is $n_{iter}=3$. A comparison of the functions of transmission errors from $n_{iter}=3$ to $n_{iter}=5$ shows that the function for $n_{iter}=3$ presents a lower peak-to-peak level than the function for $n_{iter}=4$ and the function for $n_{iter}=5$.

Figure 13 shows a comparison of the peak-to-peak level of the unloaded functions of transmission errors for the 20 reconstructed pinions where the bilateral filter is applied and for the reconstructed pinion when no filter is applied. The peak-to-peak level of transmission errors of the manufactured pinion is also illustrated by means of a black horizontal line. The shapes of the contact patterns for some reconstructed pinions are also illustrated. It is observed that for the size $r=r_n=25\,\mu$m, the level of transmission

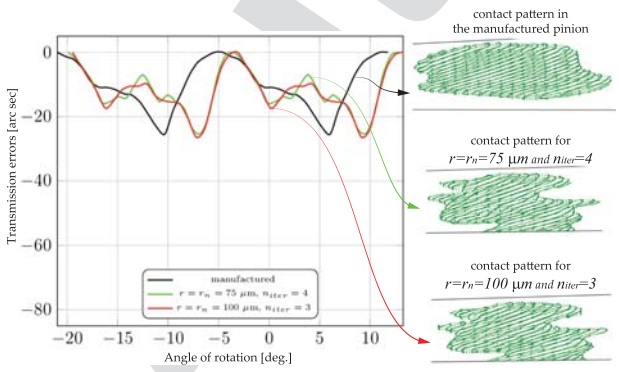

Fig. 14 Contact patterns and unloaded transmission errors for the manufactured pinion and the reconstructed pinions using the bilateral filter with $r=r_n=100\,\mu$m and $r=r_n=75\,\mu$m in mesh with the master gear

errors fluctuates along the different number of iterations and it is even larger than the level of transmission errors when no filter is applied. For the size $r=r_n=50\,\mu$m, the level of transmission errors decreases from $n_{iter}=2$ although the shape of the contact pattern is not appropriate for any number of iterations from 1 to 5 (the contact pattern for $r=r_n=50\,\mu$m and $n_{iter}=3$ is illustrated in Fig. 13 and shows holes and isolated areas over the contact pattern). For the sizes $r=r_n=75\,\mu$m and $r=r_n=100\,\mu$m, the level of transmission errors reach similar values to the manufactured pinion when $n_{iter}=3$. However, it is necessary to reach $n_{iter}=4$ for $r=r_n=75\,\mu$m to eliminate any isolated areas in the contact pattern (the contact pattern for $r=r_n=75\,\mu$m and $n_{iter}=3$ is illustrated in Fig. 13 and an isolated area is still observed in the contact pattern).

Finally, Fig. 14 shows the best results in terms of the unloaded function of transmission errors and shape of the contact patterns for the reconstructed pinions using the bilateral filter with $r=r_n=75\,\mu$m and $n_{iter}=4$ and with $r=r_n=100\,\mu$m and $n_{iter}=3$. Both contact patterns are similar to each other, without any holes or isolated areas on them. The level of transmission errors is also similar. However, the function of transmission errors for the case of $r=r_n=75\,\mu$m has more fluctuations than for the function for $r=r_n=100\,\mu$m. Both functions of transmission errors appear shifted respect to the function of transmission errors corresponding to the manufactured pinion. This shift may be due to an inaccurate location of the 5×9 micro-deviations, presented in Table 3, over the designed pinion tooth surface.

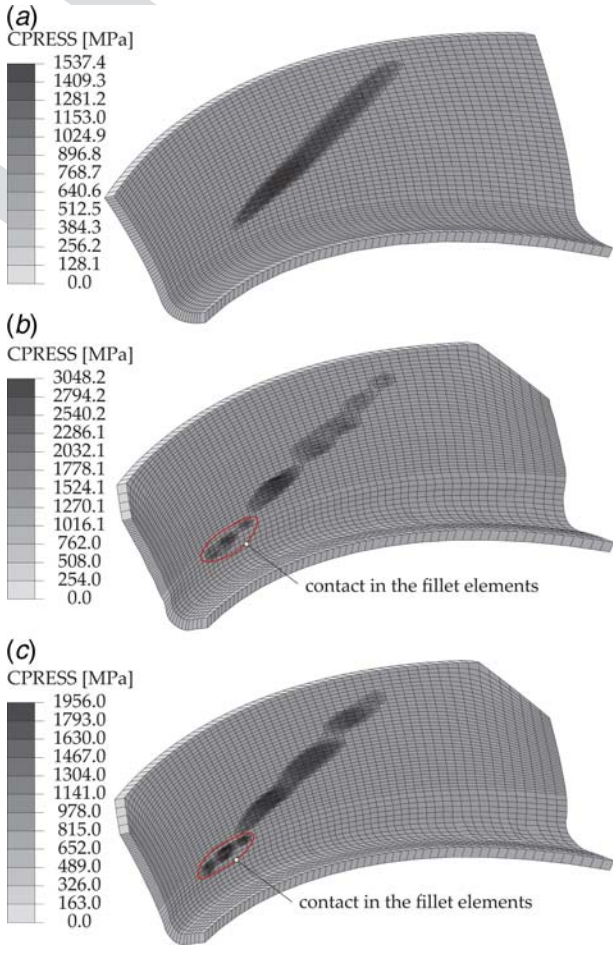

Fig. 15 Contact pressure field on the contact elements of the middle tooth of the pinion at a given step for (*a*) the manufactured geometry, (*b*) the no-filter reconstructed geometry, and (c) the reconstructed geometry with the bilateral filter using $r=r_n=100\,\mu$m and $n_{iter}=3$

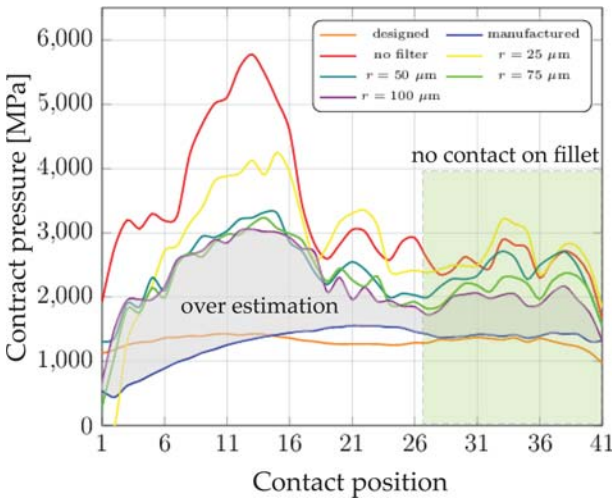

Fig. 16 Variation of contact pressure at the middle tooth of the pinion for the designed, manufactured, no-filtered and filtered reconstructed pinions using the bilateral filter with $n_{iter} = 3$

4.5 Stress Analysis. For each tooth contact analysis, a stress analysis is performed using the finite element model shown in Fig. 8. Such a model is provided with 204,500 elements and 248,304 nodes. A torque $T = 197.0$ Nm is applied at the reference node of the pinion, while the gear is held at rest at each step. A general purpose computer program (see Ref. [20]) is used for the finite element analysis. Figure 15 shows the contact pressure distribution at the same intermediate step of the stress analysis for three geometries of the pinion: the virtual manufactured one, a reconstructed geometry without application of the bilateral filter, and a reconstructed geometry with application of the bilateral filter with $r = r_n = 100$ μm and $n_{iter} = 3$. A shape very close to an ellipse is observed in Fig. 15(*a*). However, Figs. 15(*b*) and 15(*c*) show a contact area that contains isolated areas, especially when the geometry is not filtered (Fig. 15(*b*)). Although filtering improves the shape of the contact pattern (see Fig. 15(*c*)), it is not enough and the level of stresses is still higher than the one shown for the manufactured geometry (see Fig. 15(*a*)). It is also observed that some contact areas appears in the fillet area for the reconstructed pinions (see Figs. 15(*b*) and 15(*c*)) due to the impossibility to displace down the bottom edge (see Fig. 5) since no available data were provided in some areas of the point cloud below this line.

Figure 16 shows the variation of the contact pressure at the middle tooth of the pinion along 41 contact positions spread along two angular pitches of rotation of the reconstructed pinion with several types of geometry: (i) the designed and the manufactured ones provide similar level of contact pressure along two angular pitches of rotation, (ii) the reconstructed one without application of the filter shows the highest values of contact pressures, and (iii) several reconstructed geometries using the bilateral filter with $n_{iter} = 3$ and different values of radius $r = r_n$ show that the level of stresses decreases as the radius r is increased, reaching a similar level for the reconstructed geometries with $r = r_n = 75$ μm and $r = r_n = 100$ μm. Figure 16 shows in gray color the overestimation of contact pressures for the reconstructed geometry with $r = r_n = 100$ μm and $n_{iter} = 3$ respect to the manufactured geometry. Figure 16 shows as well, in green color, those contact positions where contact on fillet does not exist at the central tooth.

5 Conclusions

A methodology to reconstruct spiral bevel gears from point clouds has been proposed and applied for the virtual simulation and the analysis of reconstructed gears from filtered point clouds in terms of contact patterns and unloaded functions of transmission errors when in mesh with a master gear. Based on the performed research and results obtained, the following conclusions can be drawn:

(1) Point clouds obtained from noncontact metrology machines should be filtered before gear tooth surfaces are reconstructed for virtual simulation and analysis. The bilateral filter has been applied and their parameters r, r_n, and n_{iter} have been chosen considering the shape of the contact pattern, and the shape and peak-to-peak levels of the unloaded function of transmission errors.

(2) Contact patterns and unloaded functions of transmission errors obtained as results of tooth contact analysis with the reconstructed pinion show a satisfactory agreement with those obtained when using the reference manufactured pinion, both in mesh with the same master gear, if the appropriate parameters of the bilateral filter are chosen.

(3) Stress analysis by the finite element method reveals that the reconstructed pinion yields higher values of contact pressure than the reference manufactured pinion, mainly due to the quality of the point clouds obtained from noncontact metrology machines. Although the application of the bilateral filter helps reducing the dispersion of points in the point cloud, it is not enough to avoid high values of contact pressure in the reconstructed pinion. The missing points in the point cloud for areas close to the to-be reconstructed active tooth surface is another important factor that limits the application of the proposed methodology for the stress analysis of reconstructed gears.

Acknowledgment

The authors express their deep gratitude to the Spanish Ministry of Economy, Industry and Competitiveness (MINECO), the Spanish State Research Agency (AEI), and the European Fund for Regional Development (FEDER) for the financial support of research project DPI2017-84677-P.

Conflict of Interest

There are no conflicts of interest.

Data Availability Statement

The authors attest that all data for this study are included in the paper. No data, models, or code were generated or used for this paper.

References

[1] Kin, V., 1994, "Computerized Analysis of Gear Meshing Based on Coordinate Measurement Data," ASME J. Mech. Des., **116**(3), pp. 738–744.
[2] Fujio, H., Kubo, A., Saitoh, S., Hanaki, H., and Honda, T., 1994, "Laser Holographic Measurement of Tooth Flank Form of Cylindrical Involute Gear," ASME J. Mech. Des., **116**(3), pp. 721–729.
[3] Mahan, T., 2019, "Pulling at the Digital Thread: Exploring the Tolerance Stack Up Between Automatic Procedures and Expert Strategies in Scan to Print Processes," ASME J. Mech. Des., **141**(2).
[4] Peng, Y., Ni, K., and Goch, G., 2017, "A Real Evaluation of Involute Gear Flanks With Three-Dimensional Surface Data," American Gear Manufacturers Association Fall Technical Meeting 2017, AGMA Paper No. 17FTM08.
[5] Fuentes-Aznar, A., and Gonzalez-Perez, I., 2018, "Integrating Non-Contact Metrology in the Process of Analysis and Simulation of Gear Drives," American Gear Manufacturers Association Fall Technical Meeting 2018, AGMA Paper No. 18FTM21.
[6] Gonzalez-Perez, I., and Fuentes-Aznar, A., 2020, "Tooth Contact Analysis of Cylindrical Gears Reconstructed From Point Clouds," *New Approaches to Gear Design and Production, Mechanisms and Machine Science*, Vol. 81, Goldfarb, V., Trubachev, E., and Barmina, N., eds., Springer, New York, pp. 219–237.
[7] Hoppe, H., DeRose, T., Duchamp, T., McDonald, J., and Stuetzle, W., 1992, "Surface Reconstruction From Unorganized Points," Comput. Graph. (ACM), **26**(2), pp. 71–78.
[8] Fleishman, S., Drori, I., and Cohen-Or, D., 2003, "Bilateral Mesh Denoising," ACM SIGGRAPH 2003 Papers, SIGGRAPH '03, pp. 950–953.

[9] Tomasi, C., and Manduchi, R., 1998, "Bilateral Filtering for Gray and Color Images," Proceedings of the IEEE International Conference on Computer Vision, pp. 839–846.
[10] Digne, J., and Franchis, C. D., 2017, "The Bilateral Filter for Point Clouds," Image Process. On Line, **7**, pp. 278–287.
[11] Gill, P. E., Murray, W., and Wright, M. H., 1997, *Practical Optimization*, Academic Press, London.
[12] Nocedall, J., and Wright, S. J., 1999, *Numerical Optimization*, Springer, Berlin.
[13] Samet, H., 2006, *Foundations of Multidimensional and Metric Data Structures*, Morgan Kaufmann, San Francisco, CA.
[14] Piegl, L., and Tiller, W., 1995, *The NURBS Book*, Springer-Verlag, New York.
[15] Fuentes-Aznar, A., Iglesias-Victoria, P., Eisele, S., and Gonzalez-Perez, I., 2016, "Fillet Geometry Modeling for Nongenerated Gear Tooth Surfaces, International Conference on Power Transmissions, Chonqing, China, pp. 431–436.
[16] Sheveleva, G. I., Volkov, A. E., and Medvedev, V. I., 2007, "Algorithms for Analysis of Meshing and Contact of Spiral Bevel Gears," Mech. Mach. Theory, **42**(2), pp. 198–215.
[17] Fuentes, A., Ruiz-Orzaez, R., and Gonzalez-Perez, I., 2014, "Computerized Design, Simulation of Meshing, and Finite Element Analysis of Two Types of Geometry of Curvilinear Cylindrical Gears," Comput. Methods Appl. Mech. Eng., **272**, pp. 321–339.
[18] Gonzalez-Perez, I., and Fuentes-Aznar, A., 2017, "Analytical Determination of Basic Machine-Tool Settings for Generation of Spiral Bevel Gears and Compensation of Errors of Alignment in the Cyclo-Palloid System," Int. J. Mech. Sci., **120**, pp. 91–104.
[19] Litvin, F. L., and Fuentes, A., 2004, *Gear Geometry and Applied Theory*, Cambridge University Press, New York.
[20] Dassault Systemes, 2019, *Abaqus/Standard Analysis User's Guide*, Dassault Systemes Inc., Waltham, MA.